Tailoring the 3D Structure of Pd Nanocatalysts Supported on Mesoporous Carbon for Furfural Hydrogenation

Wu Wang,[a, b] Alberto Villa,*[c] Christian Kübel,[a, d, e] Horst Hahn,[a, b] and Di Wang*[a, d]

Abstract: By quantitative 3D structural characterization of Pd nanoparticles supported on mesoporous carbon, we identify the most important structural aspects of the catalysts, which are responsible for the activity, selectivity and stability in liquid phase furfural hydrogenation. A systematic series of catalysts were prepared by three synthetic methods: incipient wetness impregnation, wet impregnation and immobilization of preformed PVA stabilized nanoparticles in order to control the Pd nanoparticle distribution on the external and internal surfaces of the mesoporous carbon. The activity and selectivity of these catalysts are highly affected by the particle locations. More Pd nanoparticles located inside pores promote the formation of 2-methyl furan, while selectivity to furfuryl alcohol and tetrahydrofurfuryl alcohol is suppressed correspondingly. Through recycling tests we find that leaching depends on the synthesis process and plays an important role with respect to catalytic stability.

Introduction

Supported nanocatalysts are widely applied in gas and liquid phase catalytic reactions.[1,2] Porous materials are often used as catalyst support because of their high specific surface areas and controllable porous structure,[3,4] which can be used to finely tune the desired catalytic properties.[5] The distribution and location of nanoparticles supported on the porous supports has a significant effect on catalytic performance[6–8] usually due to factors such as confinement effects, transport properties, and interaction with the support surface.[9–11] For example, Serp et al. showed that PtRu nanoparticles inside carbon nanotubes are more active than the ones deposited on the external surface in cinnamaldehyde hydrogenation.[12] It was found that the selectivity of Ni/MCM-41 catalysts during pyrolysis for catalytic gasification is strongly affected by the distribution of nanoparticles.[13] When most of the particles were located inside the mesopores of MCM-41, the catalyst generated more gas, hydrogen and lower oil, compared to another catalyst where most of the particles were located on the external surface of the support.

To clarify the effect of nanoparticle location on catalytic properties and to design desired catalyst, the precise determination of the location of nanoparticle is essential. Small-angle X-ray scattering (SAXS) technique has been applied to characterize the average porosity and metal loading for catalyst particles supported on porous support.[14,15] Nevertheless, (scanning) transmission electron microscopy ((S)TEM) is one of the most employed techniques to provide spatial resolution at the nanoscale and even atomic scale, as well as the particle distribution homogeneity on individual support pieces. However, to resolve the actual location and distribution of the nanoparticle in a 3D volume quantitatively with high accuracy is still challenging. Over the last decades, electron tomography has been developed as a powerful technique to provide evidence for the specific location of nanoparticles on the support.[16–19] The works of De Jong[20–25] and Midgley[26,27] have pioneered 3D characterization of the morphology and location of small metal particles deposited inside zeolites or mesoporous networks by means of electron tomography. Using advanced image analysis, the spatial distribution of nanoparticles in porous supports, such as SBA-15, has been quantitatively studied by electron tomography[23,24] and Prieto et al. have shown that the spatial distribution of nanoparticles is an important factor for catalyst stability.[24] More recently, the preferential location of Au nanoparticles on carbon nanofibers was identified by electron tomography.[28] This study indicated that the confinement of Au NPs significantly enhances the catalytic activity and promotes selectivity towards di-acid products in polyol oxidation. These works have demonstrated that electron tomography, providing quantitative 3D information at the nanometer scale, is an invaluable tool to characterize the size, spatial distribution and exact location of nanoparticles supported on porous materials, which are indispensable to

[a] W. Wang, Dr. C. Kübel, Prof. Dr. Ing. H. Hahn, Dr. D. Wang
Institute of Nanotechnology, Karlsruhe Institute of Technology, Eggenstein Leopoldshafen (Germany)
E mail: di.wang@kit.edu
[b] W. Wang, Prof. Dr. Ing. H. Hahn
Joint Research Laboratory Nanomaterials, Technische Universität Darmstadt, Darmstadt (Germany)
[c] Dr. A. Villa
Dipartimento di Chimica, Università di Milano, Milano (Italy)
E mail: alberto.villa@unimi.it
[d] Dr. C. Kübel, Dr. D. Wang
Karlsruhe Nano Micro Facility, Karlsruhe Institute of Technology, Eggenstein Leopoldshafen (Germany)
[e] Dr. C. Kübel
Helmholtz Institute Ulm for Electrochemical Energy Storage, Karlsruhe Institute of Technology, Ulm (Germany)

understand the catalytic behavior and, in turn, to precisely design the desired catalysts.

Recently, fuel and chemical production exclusively from biomass has gained much attention due to the limited fossil fuel resources and global warming issues.[29–31] Furfural as a building block offers a rich platform for generation of biofuels[32,33] and chemical intermediates.[34] It has been identified as one of the most promising chemicals for a sustainable production in the 21st century.[35] Apart from rearrangements and furan coupling, hydrogenation is the most important process in the conversion of furfural.[34] Scheme 1 shows the
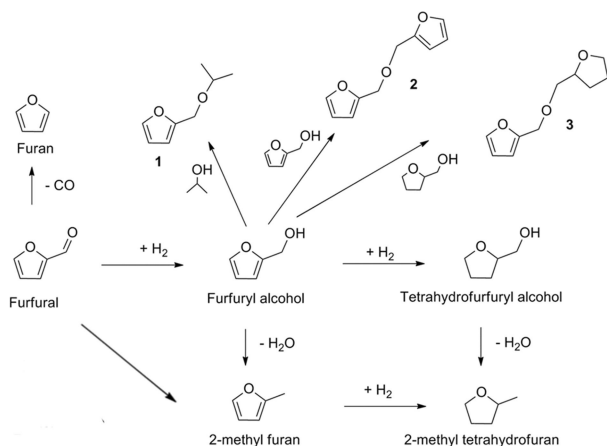
Scheme 1. Representative reaction pathways during hydrogenation of furfural.

reaction pathways of furfural hydrogenation with furfuryl alcohol as one of the most common products, which is used in the production of thermostatic resins and fiber-reinforced plastics.[29,36] Cu,[37] Ni[38] or Ru[39] based catalysts have been investigated for furfural hydrogenation and have shown good catalytic properties but under harsh reaction conditions, either at high temperature or with high hydrogen pressure. Pd is an ideal catalyst for hydrogenation of furfural because of the capability to dissociate hydrogen under ambient conditions.[40] In addition, the choice of support is also an important factor to modify the catalysts by its specific morphology and the chemical properties affecting the state of supported metal, the adsorption of reactants, and the mass transfer processes.[41,42] Porous carbons are deemed a good catalyst support material because of their high specific surface area, controllable

chemical properties of the surface and diverse porous structure,[3,4] which can be conveniently synthesized by using different polymer templates.

So far no systematic work has been performed to investigate the relationship between the spatial distribution of supported nanoparticle on porous carbons and the catalytic properties in furfural hydrogenation. In this work, we choose ordered porous CMK-3 carbon as catalyst support, which has a well-defined pore structure, to investigate the 3D distribution of Pd nanoparticles with respect to different synthetic methods and to correlate the structure of the catalysts with their activity and selectivity in furfural hydrogenation based on a quantitative tomography analysis. The Pd nanoparticles are immobilized on/in ordered mesoporous CMK-3 carbon support by three synthetic methods: incipient wetness impregnation, wet impregnation and immobilization of preformed PVA stabilized nanoparticles. The resultant spatial distributions of the Pd nanoparticles in the three Pd/CMK-3 catalysts are distinctly different from each other and effectively influence the activity and selectivity for furfural hydrogenation. The stability of the three Pd/CMK-3 catalysts is also discussed considering the preparation methods and metal-support interaction.

Results and Discussion

The results of the catalytic testing of the three 1 wt.% Pd/CMK-3 catalysts for furfural hydrogenation are summarized in Table 1 and the representative reaction pathways during hydrogenation of furfural are shown in Scheme 1. Pd_{IMP}/CMK-3 showed the best initial activity (1125 h^{-1}), compared to Pd_{PVA}/CMK-3 (750 h^{-1}) and Pd_{IW}/CMK-3 (438 h^{-1}), (Table 1). Analysis of the conversion versus time on stream revealed that after 5 hours, Pd_{PVA}/CMK-3 showed a conversion (98%) higher than that of Pd_{IMP}/CMK-3 (88%) and Pd_{IW}/CMK-3 catalysts (64%) (Figure S1). In particular, deactivation phenomena for Pd_{IMP}/CMK-3 catalyst were observed at high conversion. Furfuryl alcohol was the major product obtained in all cases (Table 1). Pd_{PVA}/CMK-3 showed a selectivity to furfuryl alcohol of 75%, higher than Pd_{IW}/CMK-3 (61%) and Pd_{IMP}/CMK-3 (56%). Tetrahydrofurfuryl alcohol was present as major secondary product when Pd_{IMP}/CMK-3 and Pd_{PVA}/CMK-3 catalysts were used (selectivity of 24% and 13%, respectively), whereas Pd_{IW}/CMK-3 also promoted the formation of methyl furan (22%). Recycling tests have been performed to investigate the durability of the catalysts (Figure 1). These tests consisted of the filtration and reuse of the

Catalyst[a]	Activity[b]	Conversion (%) after 5 h	Selectivity (%)[c] Furfuryl alcohol (FA)	Tetrahydrofurfuryl Alcohol (THFA)	2 methyl furan (MF)	Ethers		
						1	2	3
Pd_{IW}/CMK 3	438	64	61	8	22	5	nd	nd
Pd_{IMP}/CMK 3	1125	88	56	24	6	8	4	nd
Pd_{PVA}/CMK 3	750	98	75	13		7	nd	nd

Table 1. Furfural hydrogenation in 2 propanol.[a]

[a] Reaction conditions: Furfural = 0.3 M; F/catalyst ratio = 500 wt/wt, 50 °C, 5 bar H$_2$. [b] Converted mol (mol Pd)$^{-1}$ h^{-1} calculated after 15 min of reaction. [c] Selectivity calculated at 60% conversion.
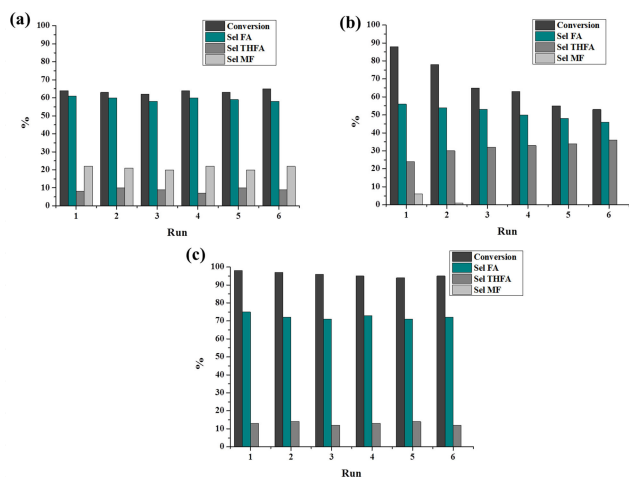
Figure 1. Stability tests running 6 reaction cycles of a) Pd_{IW}/CMK 3, b) Pd_{IMP}/CMK 3 and c) Pd_{PVA}/CMK 3 catalysts.

catalyst for the next run without any further purification. Pd_{IW}/CMK-3 and Pd_{PVA}/CMK-3 showed good stability, maintaining activity and selectivity over 6 cycles (Figure 1a and 1c). Conversely, Pd_{IMP}/CMK-3 showed an evident decrease in the conversion and continuous changes in the selectivity (Figure 1b): the selectivity to tetrahydrofurfuryl alcohol (THFA) was enhanced during cycling, while the selectivity of furfuryl alcohol (FA) and methyl furan (MF) decreased with increasing cycles.

The as-prepared Pd/CMK-3 catalysts were characterized using STEM to assess the particle size distribution. STEM images of the three catalysts and their nanoparticle size histograms are shown in Figure 2. Pd nanoparticles for the three catalysts show fairly homogeneous dispersion on the support and the Pd nanoparticle sizes of those catalysts are similar, around 2.5 nm in average with a similar size distribution. Therefore, there are clearly other factors than particle size that influence the activity and selectivity.

Electron tomography was used to quantify the number of Pd nanoparticles on the external vs. internal support surface based on the segmentation and identification of the particles in the reconstructed tomograms as outlined in the experimental section (Figure S2). Figure 3 shows representative 2D slices from the reconstructed volume of the three Pd/CMK-3 catalysts and the corresponding rendered volumes, in which surface nanoparticles are marked in yellow and the nanoparticles inside the pores are marked in red. For the Pd_{IW}/CMK-3 and Pd_{IMP}/CMK-3 catalysts, Pd nanoparticles were found both on the external surface (highlighted by yellow circles) and inside the support pores (highlighted by red-circles) while Pd nanoparticles were observed only on the external surface in case of Pd_{PVA}/CMK-3. The presence of the capping agent (PVA) increases the hydrodynamic radius of the particles, thus limiting their internal diffusion inside the channels.[28] To quantify the distribution of the particles, the percentage of particles on the external surface for each Pd/CMK-3 catalyst is calculated from several tomograms of each sample after segmentation and identification of the particles. In addition, Pd loading of individual Pd/CMK-3 particles was obtained based on the
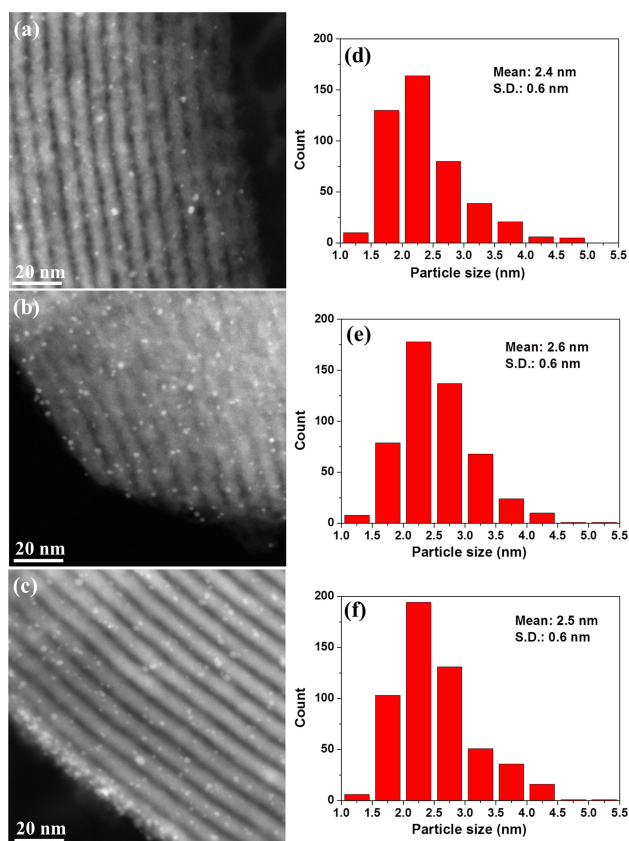

Figure 2. Representative STEM images of as prepared (a) Pd_{IW}/CMK 3, (b) Pd_{IMP}/CMK 3 and (c) Pd_{PVA}/CMK 3 catalysts and the corresponding particle size distribution histograms (d f).
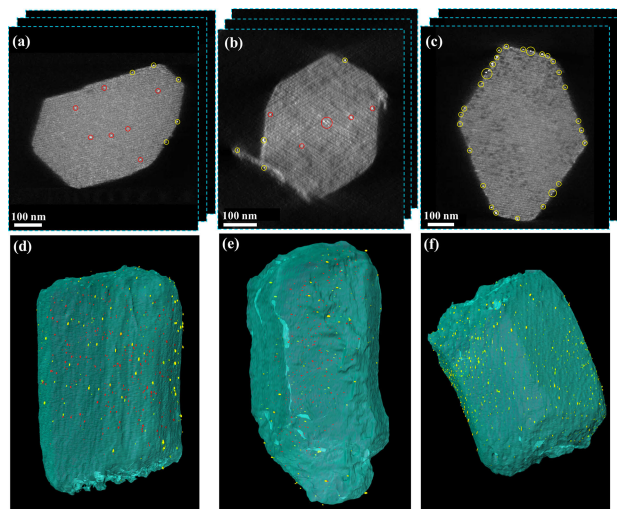

Figure 3. Typical 2D slices of (a) Pd_{IW}/CMK 3, (b) Pd_{IMP}/CMK 3 and (c) Pd_{PVA}/CMK 3 reconstruction data and the corresponding representative 3D visualization (d f). The yellow and red circles in a c highlight Pd nanoparticles on the external surface and inside of the porous support.

volume of segmented Pd nanoparticles and support (CMK-3). The resulting particle distribution and the Pd loading are summarized in Figure 4.
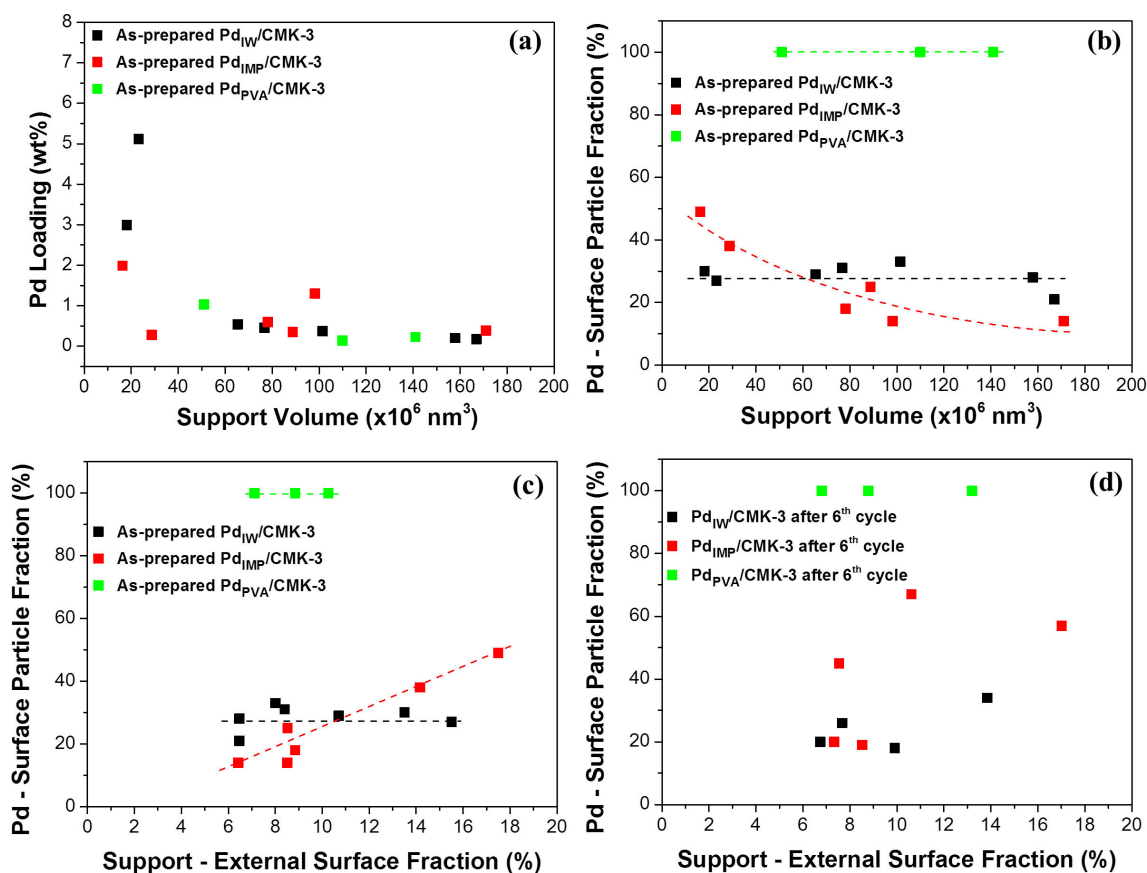
Figure 4. (a) The relationships between Pd loadings and volume of CMK 3 support. (b) Fraction of surface Pd nanoparticles to the support volume in as prepared Pd/CMK 3 catalysts, and fraction of surface Pd nanoparticles to external surface fraction of support in Pd/CMK 3 catalysts at the as prepared state (c) and after 6 cycles (d).

The dependence of the Pd loading on the support size is shown in Figure 4a. For large support pieces, the Pd loading is more or less uniform and varies slightly around the nominal loading of 1 wt.%, while the metal loading on small support pieces ($\sim 2 \times 10^7$ nm^3 or smaller) is considerably higher ($>$ 1 wt.%) for the as-prepared Pd$_{IW}$/CMK-3 and Pd$_{IMP}$/CMK-3 catalyst. The higher Pd loading on small support piece is particularly more distinct in case of Pd$_{IW}$/CMK-3, which could be due to the fact that pores in small support pieces are easier to be completely filled by the Pd precursor than in case of impregnation, where Pd precursor undergoes sufficient diffusion resulting in a more homogeneous distribution of nanoparticles. Figure 4b shows the fraction of Pd nanoparticles on the external surface for the three as-prepared Pd/CMK-3 catalysts plotted with respect to the CMK-3 support volume. About 20%–30% of Pd nanoparticles are located on the external support surface for as-prepared Pd$_{IW}$/CMK-3, almost independent on the size of the CMK-3 support, whereas in the case of as-prepared Pd$_{PVA}$/CMK-3, all Pd nanoparticles are exclusively located on the CMK-3 external surface. For as- prepared Pd$_{IMP}$/CMK-3, the amount of Pd particles on the external surface roughly decreases with the increase of the CMK-3 support volume. From the segmented tomograms, the area of the external surface and the surface area inside pores are calculated (details in Figure S3). The fraction of Pd particles located on the external surface is plotted against the fraction of the external support surface to better understand the difference of the particle distribution for IW and IMP preparation (Figure 4c). For Pd$_{IMP}$/CMK-3, the fraction of Pd nanoparticles on the external surface is proportional to the external surface fraction. This linear correlation indicates that during the impregnation process, the precursor solution has adequate time to reach the anchoring positions on both the external surface and the internal pore surfaces. However, the factor of ~ 2 between the external surface fraction and the Pd loading on the external surface indicates a higher likelihood for Pd adsorbing on the external surface compared to inside. In the contrast, during incipient wetness preparation the porous carbon support always absorbs a similar fraction of the precursor solution into the pores and always leaves 20–30% on the external surface. This means that the pores are not always completely filled, particularly for the big carbon support pieces. Small carbon pieces are more easily filled and this tendency leads to the smaller carbon support pieces with considerably higher Pd loading (Figure 4a).

A variation of the particle distribution during the catalytic reaction can be detected by comparing the tomographic analysis of the three Pd/CMK-3 catalysts at the as-prepared state and after 6 cycles (Figure 4c and 4d). For Pd$_{IW}$/CMK-3, the fraction of Pd nanoparticles on the external surface is almost

independent of the external surface fraction of the support. In addition, the absolute fraction of Pd surface nanoparticles is almost unchanged before and after catalytic reaction. This is in agreement with the observed high stability during the catalytic testing suggesting no or very limited changes during the catalytic process. For Pd_{PVA}/CMK-3 catalyst, all Pd nanoparticles still located on the external surface of the support material after reaction. Pd_{IMP}/CMK-3 underwent noticeable changes during the reaction regarding the particle distribution and the size distribution. A lot more Pd nanoparticles were observed on the external support surface after 6 reaction cycles compared to the as-prepared material.

From Figure 4b and 4c, one can estimate that the overall fraction of Pd particles on the external surface is comparable for as-prepared Pd_{IW}/CMK-3 and Pd_{IMP}/CMK-3catalysts. Therefore the high initial activity of Pd_{IMP}/CMK-3 is not directly related with the surface particle fraction and the confinement effect of the pores. A close look at the metal-support interaction and the reaction pathways may give a hint at different activities, which will be discussed later. The lower initial activity of Pd_{PVA}/CMK-3 is likely due to residual PVA stabilizing agent on the Pd nanoparticles, which might block some active sites.[43] The selectivity of furfural hydrogenation is suggested to be dependent on the binding orientation of furfural in specific types of sites (terrace sites or edges/corners sites).[44–46] Previous studies have indicated that when furfural adsorbs with a perpendicular orientation on the Pd surface, the formation of furfuryl alcohol is favored, whereas a flat-lying adsorbate on the Pd surface is prone to the formation of tetrahydrofurfuryl alcohol.[40,45] It has been shown that the presence of PVA on the Pd surface favors a perpendicular adsorption of furfural as a consequence of the interaction of the protecting agent with the NPs resulting in the formation of furfuryl alcohol.[40] On the free Pd both perpendicular and flat furfural adsorption is occurring, resulting in the formation of furfuryl alcohol and also tetrahydrofurfuryl alcohol.[45] On the contrary, the confinement inside small pores (3–4 nm) of the support can bias the reactant binding orientation to discourage flat adsorption of the reactant molecules and favors the perpendicular adsorption.[47] This configuration results in the formation of furfuryl alcohol but also of 2-methyl furan via hydrodeoxygenation (HDO) of furfuryl alcohol.[46,47] Zhang et al. have shown that furfuryl alcohol is faster hydrodeoxygenated to methyl furan when Pd nanoparticles are confined inside porous TiO_2 compared to a catalyst where Pd was mainly present on the external surface.[47] In our cases, a similar encapsulating effect is expected to work as well. In addition, it is possible that the reactants accessing the active sites through micropores of CMK-3,[48,49] which are beyond resolution of electron tomography, may further reinforce the biasing in binding directions. For encapsulated Pd catalyst a higher HDO apparent activation energy was observed, probably due to the larger concentration of Pd-support interfacial sites. Over the catalytic reaction cycles, the selectivity of Pd_{IW}/CMK-3 and Pd_{PVA}/CMK-3 catalysts remained unchanged (Figure 1a/c). In case of Pd_{IMP}/CMK-3, the selectivity of tetrahydrofurfuryl alcohol increased from 24% in the 1st cycle to 36% in the 6th cycle (Figure 1b), while the selectivity of both furfuryl alcohol

and 2-methyl furan decreased correspondingly. The change in selectivity can be correlated with the increase of the fraction of Pd nanoparticles on the external surface over the reaction cycles as can be seen comparing Figure 4c and 4d. The cycling experimental results corroborated our previously suggested mechanism that the Pd particles confined inside pores lead to a higher selectivity to furfuryl alcohol and 2-methyl furan.

Stability is of great importance for any real application of catalysts. One main reason for the deactivation of catalysts is metal nanoparticle growth causing a loss of active sites.[50] In order to measure the stability of the three catalysts, the catalytic reaction was carried out using the recycled catalysts and the structural changes were investigated by HAADF STEM. Figure 5 shows the HAADF STEM images at high magnification
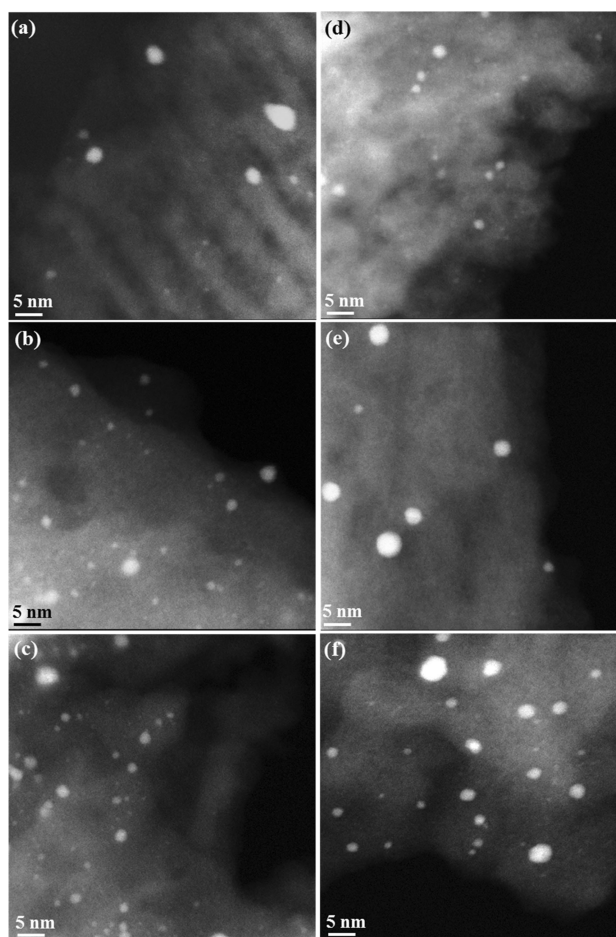

Figure 5. High resolution STEM images of Pd_{IW}/CMK 3, Pd_{IMP}/CMK 3 and Pd_{PVA}/CMK 3 catalysts in the as prepared state (a c) and after 6th cycle (d f).

of the three Pd/CMK-3 catalysts in the as-prepared state and after 6 cycles. Some ultra-small Pd nanoparticles (< 1 nm) were found in all three as-prepared Pd/CMK-3 catalysts (Figure 5a–c). After reaction, those ultra-small Pd nanoparticles almost disappeared in Pd_{IMP}/CMK-3 (Figure 5e and S5) but still remained in Pd_{IW}/CMK-3 and Pd_{PVA}/CMK-3 (Figure 5d/f and S4). Table 2 summarizes the average size of the Pd nanoparticles measured from electron tomography (3D) and STEM images

Table 2. The conversions of Pd/CMK 3 catalysts used in 1st and 6th cycle of furfural hydrogenation reaction and Pd nanoparticle sizes in the as prepared state and after 6th cycle reaction measured from electron tomography (3D) and STEM images (2D).

Catalysts	Conversion after 5 h in 1st cycle	Conversion after 5 h in 6th cycle	Average Pd nanoparticle size (nm)					
			Electron tomography (3D) as prepared		after 6th cycle		STEM (2D) as prepared	after 6th cycle
			Inside	External surface	Inside	External surface		
Pd$_{IW}$/CMK 3	64%	65%	2.4	2.9	2.3	2.9	2.4	2.4
Pd$_{IMP}$/CMK 3	88%	53%	2.6	2.9	3.7	4.6	2.6	3.8
Pd$_{PVA}$/CMK 3	98%	95%		2.7		2.8	2.5	2.6

(2D) and the corresponding catalytic conversions in the 1st and the 6th run during furfural hydrogenation. We found that the size of the Pd nanoparticles in Pd$_{IW}$/CMK-3 and Pd$_{PVA}$/CMK-3 was almost unchanged after the reaction regardless of location, whereas Pd nanoparticles obviously grew for Pd$_{IMP}$/CMK-3, especially the Pd nanoparticles on the external surface. The growth of the Pd nanoparticles in Pd$_{IMP}$/CMK-3 strongly suggests that leaching and re-deposition occurred during reaction. The leached Pd redeposits onto neighboring nanoparticles during the reaction resulting in enlarged nanoparticles, while the ultra-small Pd NPs are mostly consumed leading to the quick drop in activity of Pd$_{IMP}$/CMK-3 (Figure 1b). It is noticeable that both particle size and particle number on the external surface increased considerably during cycling reaction for Pd$_{IMP}$/CMK-3. Both can be attributed to leaching of Pd. The leached Pd is more likely to redeposit on the external surface. At the same time, Ostwald ripening likely dominates growth and the presence of unconfined Pd clusters on the outer surface provides unrestricted growth and thus an increasing driving force for ripening, which is not of the same magnitude for the NPs confined in pores. The leaching mechanism was also confirmed by checking the "hot-filtrated" solution using atomic absorption spectroscopy (AAS).[51,52] After 60 min of reaction, the catalyst was isolated by filtration without cooling the reaction mixture and ICP measurements on the filtrate evidenced that leaching of Pd loaded on CMK-3 in Pd$_{IW}$/CMK-3, Pd$_{IMP}$/CMK-3 and Pd$_{PVA}$/CMK-3 catalysts was 0.2%, 3% and 0.3%, respectively. The more prominent leaching for the impregnation prepared catalyst may be attributed to a weaker metal-support interaction. Previous studies[53,54] indicated that the pH of the solution has an effect on the electrostatic interactions between the carbon surface and the active-phase precursors. In our case, the amount of solvent (water) used in wet impregnation is much more than that used for incipient wetness impregnation. Therefore, a higher pH of the solution during wet impregnation weakens electrostatic interactions between the support CMK-3 and the Pd precursors, which could explain the evident Pd leaching and the lowest stability of Pd$_{IMP}$/CMK-3 catalyst.

Conclusions

Based on the quantitative tomographic analysis, the 3D distribution of the Pd nanoparticles of the three catalysts synthesized by incipient wetness impregnation, wet impregnation and sol immobilization methods was systematically investigated and the observed structures were correlated with their activity and selectivity in furfural hydrogenation. About 20%–30% of Pd nanoparticles are located on the external support surface for as-prepared Pd$_{IW}$/CMK-3, almost independent of the size of the CMK-3 support, whereas in case of as-prepared Pd$_{PVA}$/CMK-3, all Pd nanoparticles are exclusively located on the external CMK-3 surface. Because the accessibility of reactants to the catalyst inside the support is confined by the CMK-3 pore structure, Pd$_{IW}$/CMK-3 catalyst has a lower activity compared to Pd$_{PVA}$/CMK-3. For as-prepared Pd$_{IMP}$/CMK-3, the Pd nanoparticle fraction on the external is roughly proportional to the external surface fraction suggesting adequate time and mobility for precursors to access the anchoring sites on the internal and external surfaces. The low stability of Pd$_{IMP}$/CMK-3 could be attributed to a higher leaching rate due to weaker metal-support interaction, which was evidenced by the increasing particle size during the catalytic reaction. The location of the particles strongly influences the selectivity of the reaction. Pd nanoparticles confined in the pores of the mesoporous carbon favors the formation of 2-methyl furan, probably due to an encapsulating effect favoring perpendicular orientation of furfural adsorbed on Pd and longer contact times. When Pd nanoparticles are on the external surface the yield of tetrahydrofurfuryl alcohol becomes much higher. Moreover, the residual capping agent on Pd$_{PVA}$/CMK-3 slightly suppresses the formation of tetrahydrofurfuryl alcohol by reducing the probability of parallel adsorption binding to three Pd atoms and the absence of confinement of the particles resulted in a high selectivity to furfuryl alcohol. From the presented work, it is worth to point out that quantitative tomography was essential to understand the structural differences and thus the modulated catalytic behaviors of the three catalysts. Particularly for incipient wetness and wet impregnation prepared catalysts, quantitative analysis of the tomographic data enabled uncovering the difference in metal dispersion.

Experimental Section

Catalyst Preparation

The mesoporous carbon CMK-3 support (Nanjing XFNANO Materials Tech) has a specific surface area of ~900 m²/g and exhibits ordered porous structure with a pore diameter of 3 4 nm calculated from N_2 physisorption (Figure S5). Supported Pd/CMK-3 catalysts were prepared using incipient wetness impregnation (Pd_{IW}/CMK-3), wet impregnation (Pd_{IMP}/CMK-3) and immobilization of preformed PVA stabilized nanoparticles (Pd_{PVA}/CMK-3).

For incipient wetness impregnation, solid $Na_2PdCl_4 \cdot 2H_2O$ (Aldrich, purity 99.99%) (0.094 mmol of Pd,) was dissolved in water. Sufficient metal-containing solution was added to 1 gram of support (CMK-3) to completely fill the pores, based on the total pore volume from N_2 sorption analysis (1.24 cm³/g). The concentration of the precursor solution was calculated to obtain a final metal loading of 1 wt.%. The catalyst was filtered, re-dispersed in water and reduced with $NaBH_4$ ($Pd/NaBH_4$ 1/8 mol/mol). Afterwards the catalyst was filtered and washed several times with distilled H_2O and dried at 80 °C for 4 h.

For wet impregnation, solid Na_2PdCl_4 (0.094 mmol of Pd) was dissolved in 100 ml water. 1 gram of support (CMK-3) was added to the Na_2PdCl_4 solution under stirring. After 4 h, the catalyst was filtered, re-dispersed in water and reduced with $NaBH_4$ ($Pd/NaBH_4$ 1/8 mol/mol). The catalyst was filtered and washed several times with distilled H_2O and dried at 80 °C for 4 h.

For sol-immobilization, solid Na_2PdCl_4 (0.094 mmol of Pd) and PVA water solution (1 wt.%) (Pd/PVA 1:0.5 weight ratio) were added to 100 mL of H_2O. After 3 min, $NaBH_4$ ($Pd/NaBH_4$ 1/8 mol/mol) solution was added to the yellow-brown solution under vigorous magnetic stirring. A brown Pd(0) sol was immediately formed. An UV-visible spectrum of the Pd sol was recorded to check the complete Na_2PdCl_4 reduction. Within a few minutes from their generation, the colloid (acidified at pH 2 by sulfuric acid) was immobilized by adding the support (CMK-3) under vigorous stirring. The amount of Na_2PdCl_4 and support was calculated in order to obtain a final metal loading of 1 wt.%. The catalysts were filtered and washed several times with distilled H_2O at 60 °C to remove PVA from Pd surface and dried at 80 °C for 4 h.

Furfural Hydrogenation

Furfural (F) hydrogenation was performed at 50 °C, using a stainless steel batch reactor (30 mL capacity), equipped with heater, mechanical stirrer, gas supply system and thermometer. Furfural solution (15 mL; 0.3 M in 2-propanol) was added into the reactor and the desired amount of catalyst (F/catalyst ratio 500 wt/wt) was suspended in the solution. The H_2 pressure was set to 5 bar as optimized reaction condition while avoiding mass transport issue. The mixture was heated to the reaction temperature, 50 °C, and mechanically stirred (1250 rpm). During the reaction, samples were removed periodically (0.2 mL) and identification of the products was performed using a Thermo Scientific Trace ISQ QD Single Quadrupole GC-MS equipped with a capillary column HP-5 30 m × 0.32 mm, 0.25 × m Film, by Agilent Technologies. Quantitative analysis with an external standard method (n-octanol) was used. At the end of the reaction, the autoclave was cooled to room temperature, the H_2 flow stopped and the autoclave was purged with flowing nitrogen. Recycling tests were carried out under the same experimental conditions. The catalyst was recycled in the subsequent run after filtration without any further treatment.

Atomic Absorption Spectroscopy

Metal content and metal leaching were verified by atomic absorption spectroscopy (AAS) using a Perkin Elmer 3100.

Transmission Electron Microscopy

The powder samples of the Pd/CMK-3 catalysts were dispersed on copper grids coated with holey carbon film (Quantifoil). The morphology of the catalysts was characterized by high angle annular dark-field (HAADF) scanning transmission electron microscopy (STEM) using a FEI Titan 80 300 TEM operated at 300 kV. The size of the supported Pd nanoparticles was estimated from HAADF STEM images using ImageJ[55] software approximating the particles with an elliptical shape.

Electron Tomography and 3D Image Analysis

The powder samples of the catalysts were dispersed on 100 × 400 mesh carbon coated copper grids (Quantifoil), where 6.5 nm colloidal Au particles had been deposited beforehand. Electron tomography was performed using a Fischione 2020 tomography holder on an FEI Titan 80 300 microscope operated at an acceleration voltage of 300 kV in STEM mode with a measured beam diameter of 0.27 nm. HAADF STEM tilt series with image dimensions of 2048 × 2048 pixels were collected using the Xplore3D software (FEI) over a tilt range of at least ±70°, with tilt increments of 2°. During tilt series image acquisition no detectable morphology change caused by electron beam damage was observed. Alignment of the tilt series was performed with IMOD[56] using both Au colloidal particles and supported Pd nanoparticles as fiducial markers with a mean residual alignment error of 0.47 1.00 pixels. The aligned tilt series were reconstructed using the simultaneous iterative reconstruction technique (SIRT) within Inspect3D (FEI). The resultant tomograms had a final voxel size of 0.32 or 0.46 nm, depending on the magnification of the original STEM images.

3D image analysis and segmentation of the electron tomograms was performed in Amira 6.0. Global threshold values were applied to median-filtered reconstruction volumes to extract the features of interests, i.e., Pd nanoparticles and CMK-3 support (including pore volume), respectively. Then the segmentation of Pd nanoparticles was refined by an adaptive threshold, in which instead of fixed thresholding intensity, an adaptive threshold was set to a certain percentage of the local maximum intensity within the particle region to dynamically compute the segmentation of each individual Pd particle. Starting from the segmented CMK-3 the border was eroded by 20 voxels to detect the particles on the support surface as Pd particles in contact with vacuum (Figure S2). This erosion step is essential to avoid recognizing the intensity gradient between metal particle and vacuum as carbon. The number of nanoparticles on the external surface and inside the pores of the support was counted and the nanoparticle sizes measured as the diameter of volume-equivalent spheres. The measured volumes were corrected for the elongation factor due to the missing wedge from tomography acquisition.[57,58] Segmented Pd nanoparticles with volumes below 20 voxels were ignored during further analysis. To provide sufficient statistical sampling and to explore the influence of the size of the support on the particle distribution, several tomograms were analyzed for each catalyst after segmentation and identification of the particles to calculate the surface particle fraction and the nanoparticle size distribution. In addition, Pd loading (in wt.%) of individual Pd/CMK-3 tomogram was calculated based on the volumes derived from Pd and support (CMK-3) segmentations and the nominal overall densities of metallic Pd (12.02 g/cm³) and CMK-3 carbon (~0.6 g/cm³).

Conflict of Interest

The authors declare no conflict of interest.

Keywords: palladium nanocatalyst · electron tomography · quantitative 3D structure analysis · furfural hydrogenation · mesoporous carbon

[1] R. D. Cortright, R. R. Davda, J. A. Dumesic, *Nature* **2002**, *418*, 964 967.
[2] M. Behrens, F. Studt, I. Kasatkin, S. Kuhl, M. Havecker, F. Abild Pedersen, S. Zander, F. Girgsdies, P. Kurr, B. L. Kniep, *Science* **2012**, *336*, 893 897.
[3] Y. Yürüm, A. Taralp, T. N. Veziroglu, *Int. J. Hydrogen Energy* **2009**, *34*, 3784 3798.
[4] Y. Yang, K. Chiang, N. Burke, *Catal. Today* **2011**, *178*, 197 205.
[5] K. P. de Jong, *Synthesis of Solid Catalysts*, **2009**.
[6] A. T. Bell, *Science* **2003**, *299*, 1688 91.
[7] X. Pan, X. Bao, *Acc. Chem. Res.* **2011**, *44*, 553 562.
[8] J. P. Tessonnier, O. Ersen, G. Weinberg, C. Pham Huu, D. S. Su, R. Schlögl, *ACS Nano* **2009**, *3*, 2081 2089.
[9] L. D. Gelb, K. E. Gubbins, R. Radhakrishnan, M. Sliwinska Bartkowiak, *Reports Prog. Phys.* **2000**, *63*, 727 727.
[10] R. Valiullin, S. Naumov, P. Galvosas, J. Kärger, H. J. Woo, F. Porcheron, P. A. Monson, *Nature* **2006**, *443*, 965 968.
[11] S. Stapf, *Nat. Phys.* **2006**, *2*, 731 732.
[12] E. Castillejos, P. J. Debouttière, L. Roiban, A. Solhy, V. Martinez, Y. Kihn, O. Ersen, K. Philippot, B. Chaudret, P. Serp, *Angew. Chem. Int. Ed.* **2009**, *48*, 2529 2533; *Angew. Chem.* **2009**, *121*, 2567 2571.
[13] C. Wu, L. Dong, J. Onwudili, P. T. Williams, J. Huang, *ACS Sustainable Chem. Eng.* **2013**, *1*, 1083 1091.
[14] C. J. Gommes, G. Prieto, P. E. De Jongh, *J. Phys. Chem. C* **2016**, *120*, 1488 1506.
[15] C. J. Gommes, G. Prieto, J. Zecevic, M. Vanhalle, B. Goderis, K. P. de Jong, P. E. de Jongh, *Angew. Chem. Int. Ed. Engl.* **2015**, 11970 11974.
[16] M. Weyland, P. A. Midgley, J. M. Thomas, *J. Phys. Chem. B* **2001**, *105*, 7882 7886.
[17] P. A. Midgley, R. E. Dunin Borkowski, *Nat. Mater.* **2009**, *8*, 271 280.
[18] C. Kübel, A. Voigt, R. Schoenmakers, M. Otten, D. Su, T. C. Lee, A. Carlsson, J. Bradley, in *Microsc. Microanal.*, Cambridge University Press, **2005**, pp. 378 400.
[19] H. Friedrich, P. E. De Jongh, A. J. Verkleij, K. P. De Jong, *Chem. Rev.* **2009**, *109*, 1613 1629.
[20] A. J. Koster, U. Ziese, A. J. Verkleij, A. H. Janssen, K. P. De Jong, *J. Phys. Chem. B* **2000**, *104*, 9368 9370.
[21] A. H. Janssen, C. M. Yang, Y. Wang, F. Schüth, A. J. Koster, K. P. de Jong, *J. Phys. Chem. B* **2003**, *107*, 10552 10556.
[22] C. J. Gommes, K. De Jong, J. P. Pirard, S. Blacher, *Langmuir* **2005**, *21*, 12378 12385.
[23] H. Friedrich, J. R. A. Sietsma, P. E. De Jongh, A. J. Verkleij, K. P. De Jong, *J. Am. Chem. Soc.* **2007**, *129*, 10249 10254.
[24] G. Prieto, J. Zečević, H. Friedrich, K. P. de Jong, P. E. de Jongh, *Nat. Mater.* **2013**, *12*, 34 39.
[25] C. J. Gommes, H. Friedrich, M. Wolters, P. E. De Jongh, K. P. De Jong, *Chem. Mater.* **2009**, *21*, 1311 1317.
[26] E. P. W. Ward, T. J. V. Yates, J. J. Fernández, D. E. W. Vaughan, P. A. Midgley, *J. Phys. Chem. C* **2007**, *111*, 11501 11505.
[27] P. A. Midgley, J. M. Thomas, L. Laffont, M. Weyland, R. Raja, B. F. G. Johnson, T. Khimyak, *J. Phys. Chem. B* **2004**, *108*, 4590 4592.
[28] A. Villa, D. Wang, C. E. Chan Thaw, S. Campisi, G. M. Veith, L. Prati, *Catal. Sci. Technol.* **2016**, *6*, 598 601.
[29] A. Corma Canos, S. Iborra, A. Velty, *Chem. Rev.* **2007**, *107*, 2411 2502.
[30] M. Besson, P. Gallezot, C. Pinel, *Chem. Rev.* **2014**, *114*, 1827 1870.
[31] A. J. Ragauskas, C. K. Williams, B. H. Davison, G. Britovsek, J. Cairney, C. A. Eckert, W. J. Frederick, J. P. Hallett, D. J. Leak, C. L. Liotta, *Science* **2006**, *311*, 484 9.
[32] K. Yan, G. Wu, T. Lafleur, C. Jarvis, *Renewable Sustainable Energy Rev.* **2014**, *38*, 663 676.
[33] G. W. Huber, S. Iborra, A. Corma, *Chem. Rev.* **2006**, *106*, 4044 4098.
[34] J. P. Lange, E. Van Der Heide, J. Van Buijtenen, R. Price, *ChemSusChem* **2012**, *5*, 150 166.
[35] J. J. Bozell, G. R. Petersen, *Green Chem.* **2010**, *12*, 539.
[36] J. B. Barr, S. B. Wallon, *J. Appl. Polym. Sci.* **1971**, *15*, 1079 1090.
[37] R. S. Rao, R. Terry, K. Baker, M. A. Vannice, *Catal. Lett.* **1999**, *60*, 51 57.
[38] Y. Nakagawa, H. Nakazawa, H. Watanabe, K. Tomishige, *ChemCatChem* **2012**, *4*, 1791 1797.
[39] P. Panagiotopoulou, N. Martin, D. G. Vlachos, *J. Mol. Catal. A* **2014**, *392*, 223 228.
[40] S. M. Rogers, C. R. A. Catlow, C. E. Chan Thaw, A. Chutia, N. Jian, R. E. Palmer, M. Perdjon, A. Thetford, N. Dimitratos, A. Villa, *ACS Catal.* **2017**, *7*, 2266 2274.
[41] S. Nishimura, *Handbook of Heterogeneous Catalytic Hydrogenation for Organic Synthesis*, **2001**.
[42] H. F. Rase, *Handbook of Commercial Catalysts: Heterogeneous Catalysts*, **2000**.
[43] A. Villa, D. Wang, G. M. Veith, F. Vindigni, L. Prati, *Catal. Sci. Technol.* **2013**, *3*, 3036.
[44] S. H. Pang, C. A. Schoenbaum, D. K. Schwartz, J. W. Medlin, *ACS Catal.* **2014**, *4*, 3123 3131.
[45] S. H. Pang, C. A. Schoenbaum, D. K. Schwartz, J. W. Medlin, *Nat. Commun.* **2013**, *4*, 2448.
[46] V. Vorotnikov, G. Mpourmpakis, D. G. Vlachos, *ACS Catal.* **2012**, *2*, 2496 2504.
[47] J. Zhang, B. Wang, E. Nikolla, J. W. Medlin, *Angew. Chem. Int. Ed.* **2017**, *56*, 6594 6598; *Angew. Chem.* **2017**, *129*, 6694 6698.
[48] A. Taguchi, F. Schüth, *Ordered Mesoporous Materials in Catalysis*, **2005**.
[49] L. A. Solovyov, A. N. Shmakov, V. I. Zaikovskii, S. H. Joo, R. Ryoo, *Carbon N. Y.* **2002**, *40*, 2477 2481.
[50] P. Wynblatt, N. A. Gjostein, *Prog. Solid State Chem.* **1975**, *9*, 21 58.
[51] R. Liu, Y. Shi, Y. Wan, Y. Meng, F. Zhang, D. Gu, Z. Chen, B. Tu, D. Zhao, *J. Am. Chem. Soc.* **2006**, *128*, 11652 11662.
[52] C. E. Chan Thaw, A. Villa, L. Prati, A. Thomas, *Chem. Eur. J.* **2011**, *17*, 1052 1057.
[53] F. Coloma, A. Sepúlveda Escribano, J. L. G. Fierro, F. Rodríguez Reinoso, *Langmuir* **1994**, *10*, 750 755.
[54] P. Serp, J. L. Figueiredo, *Carbon Materials for Catalysis*, **2009**.
[55] J. Schindelin, I. Arganda Carreras, E. Frise, V. Kaynig, M. Longair, T. Pietzsch, S. Preibisch, C. Rueden, S. Saalfeld, B. Schmid, *Nat. Methods* **2012**, *9*, 676 682.
[56] J. R. Kremer, D. N. Mastronarde, J. R. McIntosh, *J. Struct. Biol.* **1996**, *116*, 71 6.
[57] M. Radermacher, W. Hoppe, in *7th Eur. Congr. El. Micr.* **1980**, pp. 132 133.
[58] C. Kübel, D. Niemeyer, R. Cieslinski, S. Rozeveld, *Mater. Sci. Forum* **2010**, *638 642*, 2517 2522.